



## Ballistic spin-transport properties of magnetic tunnel junctions with MnCr-based ferrimagnetic quaternary Heusler alloys

Tufan Roy <sup>1,\*</sup>, Masahito Tsujikawa,<sup>2</sup> and Masafumi Shirai <sup>1,2</sup>

<sup>1</sup>Center for Science and Innovation in Spintronics, Core Research Cluster, Tohoku University, Sendai 980-8577, Japan

<sup>2</sup>Research Institute of Electrical Communication, Tohoku University, Sendai 980-8577, Japan



(Received 25 July 2023; accepted 9 October 2023; published 25 October 2023)

We investigate the suitability of nearly half-metallic ferrimagnetic quaternary Heusler alloys,  $\text{CoCrMnZ}$  ( $Z = \text{Al, Ga, Si, Ge}$ ), to assess their feasibility as electrode materials for  $\text{MgO}$ -based magnetic tunnel junctions (MTJs). The low magnetic moments of these alloys originating from the antiferromagnetic coupling between Mn and Cr spins ensure a negligible stray field in spintronics devices as well as a lower switching current required to flip their spin direction. We confirmed the mechanical stability of these materials with the evaluated values of elastic constants and by the absence of any imaginary frequency in their phonon dispersion curves. The influence of swapping disorders on the electronic structures and their relative stability is also discussed. High spin polarization of the conduction electrons is observed in the case of  $\text{CoCrMnZ}/\text{MgO}$  heterojunctions, independent of terminations at the interface. Based on our ballistic transport calculations, large coherent tunneling of the majority-spin  $s$ -like  $\Delta_1$  states can be expected through the  $\text{MgO}$  barrier. The calculated tunneling magnetoresistance (TMR) ratios are on the order of 1000%. Very high Curie temperatures specifically for  $\text{CoCrMnAl}$  and  $\text{CoCrMnGa}$ , which are comparable to bcc Co, could also yield a weaker temperature dependence of TMR ratios for  $\text{CoCrMnAl}/\text{MgO}/\text{CoCrMnAl}$  (001) and  $\text{CoCrMnGa}/\text{MgO}/\text{CoCrMnGa}$  (001) MTJs.

DOI: [10.1103/PhysRevMaterials.7.104410](https://doi.org/10.1103/PhysRevMaterials.7.104410)

### I. INTRODUCTION

Spin-dependent transport properties of electrons have been attracting much attention from researchers for both practical applications and basic physics. In spintronics, in addition to the charge current of electrons, the spin currents are utilized in various device applications to reduce energy consumption. Magnetic tunnel junctions (MTJs) are key elements of spintronic devices, such as nonvolatile memory [1–3]. In MTJs, two magnetic electrodes are separated by an insulating barrier. If the magnetic materials have their magnetization directions parallel (antiparallel) to each other, the junction provides lower (higher) resistance. The tunneling magnetoresistance (TMR) ratio is proportional to the difference in resistance between the parallel and antiparallel magnetization configurations. A high TMR ratio is desirable in many applications such as magnetoresistive random access memory (MRAM), neuromorphic devices, medical applications, and so on [4–6].

In the search for suitable electrode materials with a high TMR ratio, different classes of materials have been studied. Heusler alloys are one of these popular classes of materials which are being used as electrode materials. Many Co-based Heusler alloys have been reported to show half-metallic electronic structure, for which 100% spin-polarized conduction electrons are achievable theoretically [7–9]. Furthermore, Co-based Heusler alloys show a very high Curie temperature  $T_C$ , which is also an essential physical entity for potential electrode materials. The most studied MTJ with Heusler

alloy electrodes is  $\text{Co}_2\text{MnSi}/\text{MgO}/\text{Co}_2\text{MnSi}$  [10–13]. It has a TMR ratio higher than 2000% at low temperatures, although the TMR ratio diminishes rapidly at room temperature (354%) [14]. The high TMR ratio at lower temperature can be explained as being a consequence of coherent tunneling of  $\Delta_1$  electrons through the  $\text{MgO}$  barrier and the half-metallic electronic structure of  $\text{Co}_2\text{MnSi}$  [15–17].

However, it is, indeed, a challenge for researchers to have a weaker temperature dependence of the TMR ratio. To date, bcc Co/ $\text{MgO}$ /bcc Co has relatively weak temperature dependence on the TMR ratio owing to very high  $T_C$  [18]. Recently, bcc  $\text{Co}_3\text{Mn}/\text{MgO}/\text{bcc Co}_3\text{Mn}$  and bcc  $\text{CoFeMn}/\text{MgO}/\text{bcc CoFeMn}$  electrodes were also reported to have a lower temperature dependence of the TMR ratio [19–22].

In magnetization switching devices such as spin-transfer-torque (STT) MRAM and spin-orbit-torque (SOT) MRAM, the switching current, which is proportional to the value of the magnetization of the free layer, needs to be reduced to decrease the power consumption. Thus, ferrimagnetic Heusler alloys could be a promising candidate to investigate. Apart from conventional Co-based ternary Heusler alloys, extensive investigations have been carried out for quaternary Heusler alloys owing to their diversity and the tunability of their electronic and magnetic properties [23–27]. Recently, we investigated the Mn-Cr-based ferrimagnetic Heusler alloys  $\text{IrCrMnZ}$  ( $Z = \text{Al, Ga, Si, Ge}$ ) [27]. We showed that the nearest neighboring Mn and Cr possess strong antiferromagnetic exchange coupling, which leads to high  $T_C$ . In  $\text{IrCrMnZ}$ , the replacement of Ir by Co will result in a shorter lattice parameter, leading to a much stronger Mn-Cr exchange coupling and thus a higher  $T_C$ . Another issue with  $\text{IrCrMnZ}$  is that Ir

\*roy.tufan.a3@tohoku.ac.jp

is an expensive and rare element, and thus, there could be a practical obstacle in mass production.

In this study, we theoretically investigate the quaternary Heusler alloys  $\text{CoCrMnZ}$  ( $Z = \text{Al, Ga, Si, Ge}$ ). These materials are ferrimagnetic with very high  $T_C$  and have reasonable lattice matching with  $\text{MgO}$ . Previously,  $\text{CoCrMnAl}$  was synthesized in its bulk form [28]. However, its heterojunction with  $\text{MgO}$  has not been studied so far. In this study, we confirm the stability of the bulk phases of  $\text{CoCrMnZ}$ , and then we study the electronic and magnetic properties of  $\text{CoCrMnZ}/\text{MgO}$  (001) heterojunctions on the basis of the density-functional calculation. Finally, we theoretically investigate the ballistic transport properties of  $\text{CoCrMnZ}/\text{MgO}/\text{CoCrMnZ}$  MTJs.

## II. METHOD

We carried out structural optimization of bulk  $\text{CoCrMnZ}$  alloys using the Vienna Ab initio Simulation Package (VASP) [29,30] combined with the projector augmented wave method [31]. We used generalized-gradient-approximation (GGA) for the exchange-correlation energy [32]. For the Brillouin zone integration, we used a  $k$  mesh of  $16 \times 16 \times 16$ . With the optimized structure of bulk  $\text{CoCrMnZ}$ , we formed a  $\text{CoCrMnZ}(11 \text{ ML})/\text{MgO}(n \text{ ML})$  heterojunction ( $n = 5, 7, 9$ , ML = monolayer) along the (001) direction, in which the  $\text{CoCrMnZ}$  unit cell is rotated by  $45^\circ$  around the  $z$  axis. The atomic positions in the heterojunction were relaxed in the  $z$  direction, keeping the in-plane lattice parameter fixed to the equilibrium lattice parameter of bulk  $\text{CoCrMnZ}$ . During structural optimization, we used a  $10 \times 10 \times 1$   $k$  mesh, and a denser  $16 \times 16 \times 2$   $k$  mesh was used to achieve the magnetic moments and density of states. We used a plane-wave cutoff energy of 500 eV in all the calculations using VASP.

To study the dynamical stability of bulk  $\text{CoCrMnZ}$ , we carried out phonon dispersion calculations. A small-displacement method was used for this calculation as implemented in the PHONOPY code [33,34] and interfaced with VASP. Here, we used a  $4 \times 4 \times 4$  supercell, which contains 256 atoms. The influence of swapping disorder was investigated using a  $2 \times 2 \times 2$  supercell which includes 128 atoms. The chemical disorder of constituent atoms was taken into account by adopting special quasirandom structures (SQSs) as implemented in the Alloy-Theoretic Automated Toolkit (ATAT) package [35,36].

For the calculations of  $T_C$ , we employ a mean-field approximation after evaluating Heisenberg exchange coupling constants using Liechtenstein's formalism [37]. First, we perform self-consistent-field calculations using the spin-polarized relativistic Korringa-Kohn-Rostoker package (SPR-KKR) [38]. We used a full potential mode, and the angular momentum expansion of the basis function was limited to  $l_{\text{max}} = 3$ . For the integration in the Brillouin zone, we used 917 irreducible  $k$  points. All the calculations were performed in scalar-relativistic representation for the valence electrons, where spin-orbit coupling was ignored. The Fermi energy was determined using Llyod's formula [39,40]. Note that for the evaluation of  $T_C$  we used both GGA [32] and the local-density approximation (LDA) [41,42] for the exchange-correlation functional.

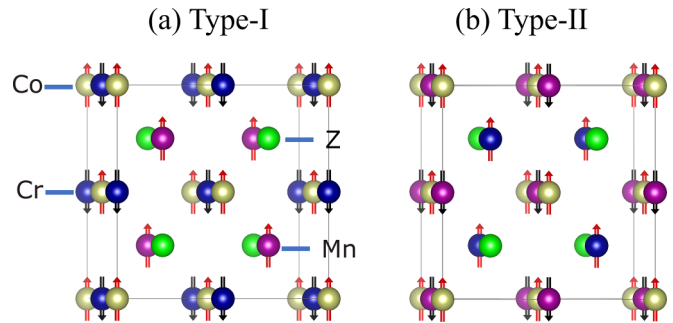


FIG. 1. Schematic illustration of  $\text{CoCrMnZ}$  ( $Z = \text{Al, Ga, Si, Ge}$ ) Heusler alloys for (a) type-I and (b) type-II structures. Arrows indicate the direction of spin vectors of the magnetic atoms in the respective structures. The structures were visualized using VESTA [46].

Finally, we studied the ballistic transport properties of the  $\text{CoCrMnZ}/\text{MgO}/\text{CoCrMnZ}$  (001) MTJ using the PWCOND code as implemented in the QUANTUM ESPRESSO package [43–45]. For the self-consistent-field calculations, we used a  $k$  mesh of  $12 \times 12 \times 1$  and an energy cutoff of 500 Ry for the charge density and 50 Ry for the wave function. The spin-resolved and in-plane wave vector [ $k_{\parallel} = (k_x, k_y)$ ] resolved conductance were calculated from the converged charge density in parallel and antiparallel magnetizations. Thereafter, we obtained the average conductances  $G_{P,\text{maj}}$ ,  $G_{P,\text{min}}$ ,  $G_{AP,\text{maj}}$ , and  $G_{AP,\text{min}}$  for both majority- and minority-spin electrons in parallel and antiparallel magnetizations, for example,  $G_{P,\text{maj}} = \frac{1}{N} \sum_{k_{\parallel}} G_{P,\text{maj}}(k_{\parallel})$ , where  $N$  is the number of sampling points in the  $k_x$ - $k_y$  plane, which is set to  $100 \times 100$  in our calculations. We similarly obtained  $G_{P,\text{min}}$ ,  $G_{AP,\text{maj}}$ , and  $G_{AP,\text{min}}$ . The TMR ratio is evaluated from the following formula:  $\text{TMR ratio} (\%) = (G_P - G_{AP})/G_{AP} \times 100$ , where  $G_P = G_{P,\text{maj}} + G_{P,\text{min}}$  and  $G_{AP} = G_{AP,\text{maj}} + G_{AP,\text{min}}$ .

## III. RESULTS

### A. Bulk phase

#### 1. Crystal structure

Quaternary Heusler alloys have the chemical formula  $XX'YZ$ , where  $X$ ,  $X'$ , and  $Y$  are the transition-metal elements and  $Z$  are the main-group  $sp$  elements. In the ordered cubic phase, these alloys belong to space group  $F\bar{4}3m$  (No. 216). There are four atomic sites:  $A$  (0, 0, 0),  $B$  (0.5, 0.5, 0.5),  $C$  (0.25, 0.25, 0.25), and  $D$  (0.75, 0.75, 0.75). First, we consider two different types of configurations as follows: (I) a Cr atom at the  $B$  site and a Mn atom at the  $C$  site (II) a Mn atom at the  $B$  site and a Cr atom at the  $C$  site; in both of these configurations Co and Z atoms occupy the  $A$  and  $D$  sites, respectively. Figure 1 presents the considered crystal structure and the direction of the spin moments of the magnetic atoms.

Figure 2 shows the total energy  $\Delta E$  of  $\text{CoCrMnZ}$  as a function of the lattice parameter  $a$  for type-I and type-II structures. Note that the origin of the vertical axis is set to the total energy of the type-I structure at its equilibrium lattice parameter. We find that except for  $\text{CoCrMnAl}$ , the systems have type-I crystal structure as their lowest energy configuration. However, the type-II structure of  $\text{CoCrMnAl}$  has a slightly lower energy

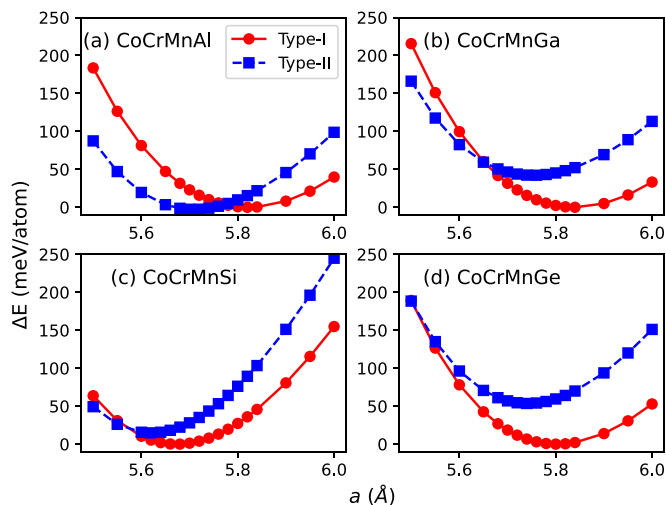


FIG. 2. Total energy as a function of the lattice parameter for (a) CoCrMnAl, (b) CoCrMnGa, (c) CoCrMnSi, and (d) CoCrMnGe. In the type-I (type-II) configuration the magnetic moment of the Cr (Mn) atom has antiparallel alignment with respect to the Co and Mn (Cr) atoms.

than its type-I configuration ( $\Delta E = -2.61$  meV/atom). Note that the equilibrium lattice parameter of CoCrMnAl in the type-II configuration (5.70 Å) is remarkably shorter than its value in the type-I configuration (5.82 Å). According to the preceding reports [28,47], the experimental lattice parameter of CoCrMnAl is 5.78 Å, which is much closer to the type-I configuration. Thus, we consider the type-I structure for all CoCrMnZ ( $Z = \text{Al, Ga, Si, Ge}$ ) hereafter.

## 2. Stability analysis

**Electronic stability.** In this section we discuss the stability of CoCrMnZ in terms of the formation energy  $E_f$  and the phase separation energy  $\delta E$ . The formation energy of a multicomponent alloy signifies its stability against decomposition into the equilibrium phases of constituent elements. On the other hand, the phase separation energy of an alloy signifies its stability against decomposition into other alloys and/or elemental phases of constituent atoms. For any energetically stable alloys under equilibrium conditions, it is necessary that both  $E_f$  and  $\delta E$  are negative. We summarize the values of  $E_f$  and  $\delta E$  in Table I. We find that for all cases  $E_f$  is negative, while  $\delta E$  is marginally positive. Possible competing phases are also listed in Table I. According to Gao *et al.* [48], a quaternary Heusler alloy with a positive phase sep-

TABLE I. Formation energy  $E_f$  and phase separation energy  $\delta E$ , along with competing phases of CoCrMnZ.

Material	$E_f$ (eV/atom)	$\delta E$ (eV/atom)	Competing phases
CoCrMnAl	-0.19	+0.11	AlCo, Cr, Mn
CoCrMnGa	-0.12	+0.04	CoGa, Mn <sub>2</sub> CoGa, Cr
CoCrMnSi	-0.33	+0.06	Co <sub>2</sub> MnSi, Cr <sub>3</sub> Si, Mn <sub>3</sub> Si
CoCrMnGe	-0.15	+0.04	Co <sub>2</sub> MnGe, Cr <sub>3</sub> Ge, Mn <sub>3</sub> Ge

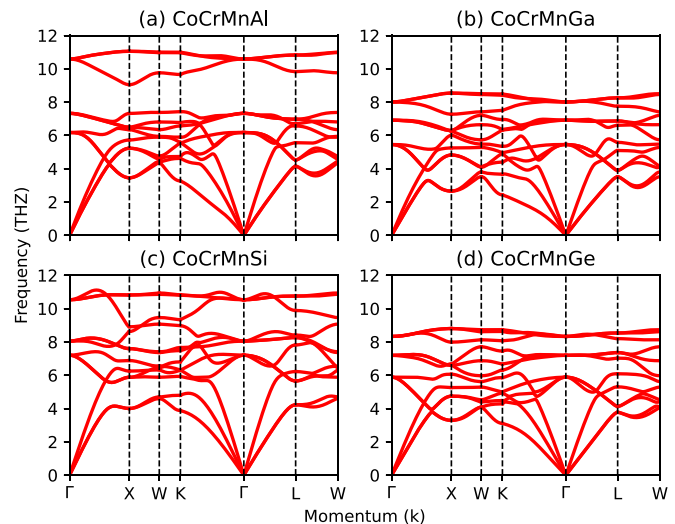


FIG. 3. Phonon dispersion curves for (a) CoCrMnAl, (b) CoCrMnGa, (c) CoCrMnSi, and (d) CoCrMnGe.

aration energy of around 0.1 eV/atom could be synthesized in experiment. For instance, although CoFeCrAl has a phase separation energy of 0.114 eV/atom, this material was synthesized as thin films by several experimental groups [23,49]. Thus, we believe that the family of CoCrMnZ alloys could be grown successfully in experiment. Indeed, CoCrMnAl was already synthesized in bulk [28,47,50]. Furthermore, in this study we focus on the spin-dependent transport properties of CoCrMnZ/MgO/CoCrMnZ (001) MTJs, in which CoCrMnZ could be grown as thin films under appropriate nonequilibrium conditions.

**Mechanical stability.** Here, we confirm the mechanical stability of CoCrMnZ in terms of elastic constants and phonon dispersion curves. For any cubic solid there are three independent elastic constants,  $C_{11}$ ,  $C_{12}$ , and  $C_{44}$ . The stability criteria of the cubic phase are as follows:  $C_{11} > 0$ ,  $C_{44} > 0$ ,  $C_{11} - C_{12} > 0$ , and  $C_{11} + C_{12} > 0$ . As listed in Table II, all the materials considered here satisfy these criteria. Thus, we conclude that these materials are mechanically stable. We also evaluate bulk and shear moduli, following the Voigt formalism [54]. We find that both bulk and shear moduli are also positive for CoCrMnZ and the values are comparable with those for bcc Fe.

The phonon dispersion curves of CoCrMnZ are presented in Fig. 3 to discuss the dynamical stability. For a system which has an instability against lattice deformation, imaginary frequencies appear in the phonon dispersion curves. For instance, Ni<sub>2</sub>MnGa and Mn<sub>2</sub>NiGa, which are well known to undergo a structural transition from the high temperature cubic phase, show a softening in phonon dispersion curves, implying the instability of the cubic phase [55,56]. As found in Fig. 3, all the phonon modes of these materials have real frequencies. Thus, we conclude that the cubic structures of all these materials are dynamically stable.

## 3. Electronic structure

In Fig. 4 we present the electronic band dispersion along the high-symmetry directions and the density of states

TABLE II. Elastic constants of CoCrMnZ. Values for CoCrMnSi and bcc Fe from previous experiments or calculations are presented for the sake of comparison.

Material	$C_{11}$ (GPa)	$C_{12}$ (GPa)	$C_{44}$ (GPa)	Bulk modulus (GPa)	Shear modulus (GPa)
CoCrMnAl	195	110	114	138	85
CoCrMnGa	189	120	109	143	79
CoCrMnSi	261, 256 <sup>a</sup>	152, 148 <sup>a</sup>	130, 130 <sup>a</sup>	188, 184 <sup>a</sup>	100, 91 <sup>a</sup>
CoCrMnGe	211	131	112	157	83
bcc Fe	277, 271 <sup>b</sup> , 243 <sup>c</sup>	132, 145 <sup>b</sup> , 138 <sup>c</sup>	89, 101 <sup>b</sup> , 122 <sup>c</sup>	180, 187 <sup>b</sup> , 173 <sup>c</sup>	82, 86 <sup>b</sup> , 94 <sup>c</sup>

<sup>a</sup>Reference [51] (theoretical result).<sup>b</sup>Reference [52] (theoretical result).<sup>c</sup>Reference [53] (experimental result).

(DOS) for CoCrMnAl and CoCrMnGa. For CoCrMnAl and CoCrMnGa the DOSs at the Fermi level  $E_F$  in the majority-spin channel are 2.47 and 1.92 states/eV per formula unit, respectively. On the other hand, there are hole pockets at the top of the valence band around the  $\Gamma$  point in the minority-spin channel, leading to smaller DOSs at  $E_F$ , i.e., 0.16 and 0.25 states/eV per formula unit for CoCrMnAl and CoCrMnGa, respectively. As a result, the values of spin polarization are 88% and 77%, respectively, for CoCrMnAl and CoCrMnGa. Figure 5 depicts the electronic band dispersion and the DOSs of CoCrMnSi and CoCrMnGe. These two materials also show metallic behavior for the majority-spin channel, although the DOSs at  $E_F$  are much smaller than those of CoCrMnAl and CoCrMnGa. The values of the majority-spin DOSs at  $E_F$  are 0.6 and 1.6 states/eV per formula unit for CoCrMnSi and CoCrMnGe, respectively. However, the minority-spin DOS almost vanishes for both CoCrMnSi and CoCrMnGe, leading to very high spin polarizations of the conducting electrons, which are approximately 100% for CoCrMnSi and 92% for CoCrMnGe.

In both Figs. 4 and 5, we mark the totally symmetric  $\Delta_1$  band by a black arrow in the majority-spin channel along the  $\Gamma$ - $X$  direction ( $\Delta$  line). The  $\Delta_1$  band is predominantly composed of  $s$ ,  $p_z$ , and  $d_{z^2}$  orbitals of Co, Cr, and Mn atoms. It has been reported that in MgO-based MTJs the  $\Delta_1$  electrons have the slowest decay rate through the MgO barrier, which originates from the complex band structure of MgO. Thus, the

presence of  $\Delta_1$  electrons in the majority-spin channel plays a pivotal role in obtaining a large transmission and low resistance area product in the parallel magnetization configuration of the MTJs.

### B. Magnetic properties

CoCrMnZ ( $Z = \text{Al, Ga, Si, Ge}$ ) have a ferrimagnetic ground state, in which the spin moments of Cr atoms have opposite directions with respect to the Co and Mn spin moments as we observe from Table III. A strong antiferromagnetic exchange coupling between the nearest neighboring Cr and Mn spins stabilizes the ferrimagnetic ground state. It should be noted that the total magnetic moments of half-metallic full Heusler alloys obey the Slater-Pauling rule [9]; that is, the total magnetic moment  $\mu_{\text{total}}$  is related to the valence electron number  $N_v$  as follows:

$$\mu_{\text{total}} = N_v - 24. \quad (1)$$

In CoCrMnAl and CoCrMnGa, the value of  $N_v$  is 25, and it becomes 26 for CoCrMnSi and CoCrMnGe. A slight deviation from the Slater-Pauling rule found in CoCrMnZ results in the reduction of spin polarization from its ideal value of 100%.

A high TMR ratio in a MTJ with a MgO barrier is generally ensured if the electrode material has a partially occupied  $\Delta_1$  band in only one spin channel owing to the coherent tunneling [15,16]. However, the TMR ratio at room temperature is

TABLE III. Calculated magnetic moments of CoCrMnZ and the equilibrium lattice parameter  $a_{\text{opt}}$ .

Material	$a_{\text{opt}}$ ( $\text{\AA}$ )	$\mu_{\text{total}}$ (in units of $\mu_B$ )	$\mu_{\text{Co}}$ (in units of $\mu_B$ )	$\mu_{\text{Cr}}$ (in units of $\mu_B$ )	$\mu_{\text{Mn}}$ (in units of $\mu_B$ )
CoCrMnAl	5.822, 5.823 <sup>a</sup>	1.02, 1.02 <sup>a</sup>	0.67, 0.69 <sup>a</sup>	-2.39, -1.32 <sup>a</sup>	2.80, 2.76 <sup>a</sup>
CoCrMnGa	5.840	1.08	0.70	-2.49	2.90
CoCrMnSi	5.672, 5.679 <sup>b</sup>	1.99, 2.01 <sup>b</sup>	0.77, 0.91 <sup>b</sup>	-1.42, -1.35 <sup>b</sup>	2.63, 2.57 <sup>b</sup>
CoCrMnGe	5.803	2.01	0.85	-1.79	2.90

<sup>a</sup>Reference [50].<sup>b</sup>Reference [51].

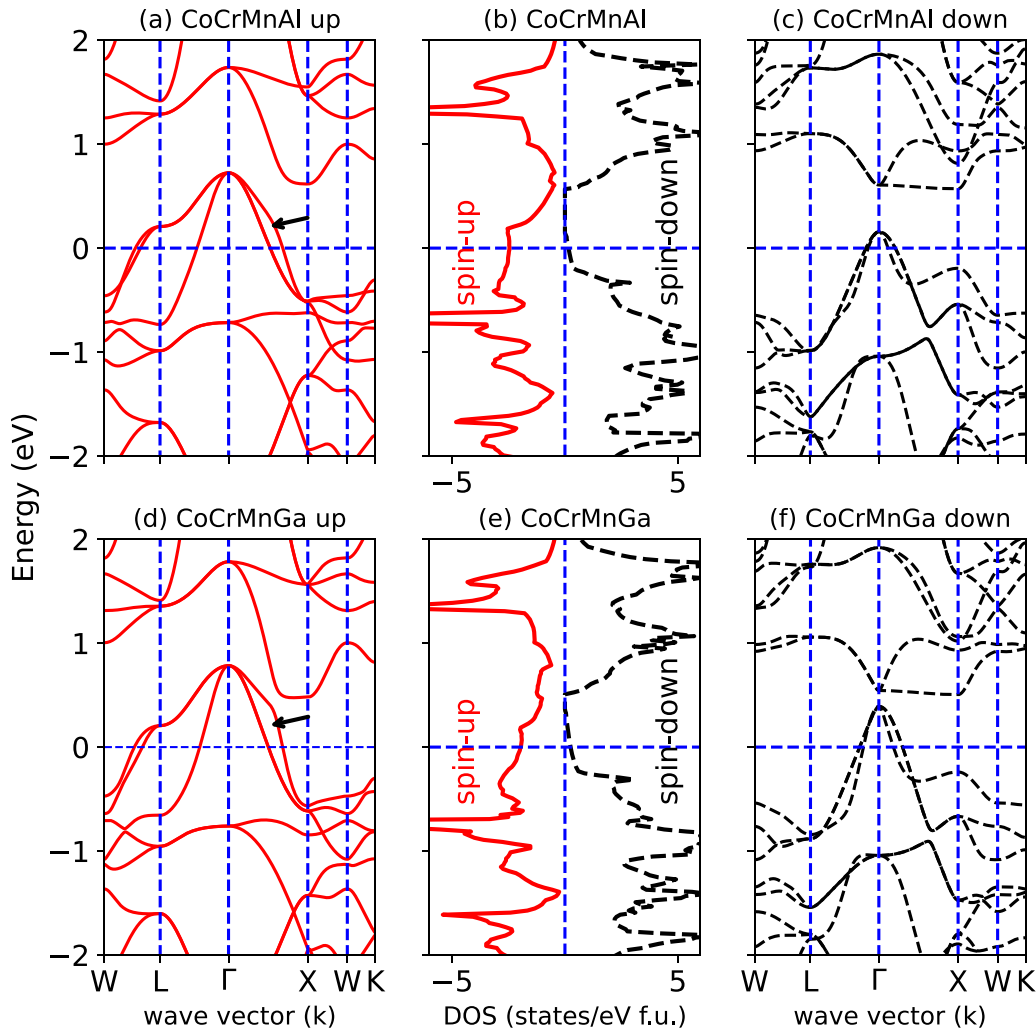


FIG. 4. Band dispersion curves and density of states for (a)–(c) CoCrMnAl and (d)–(f) CoCrMnGa, respectively. Black arrows in (a) and (d) indicate the electronic band with  $\Delta_1$  symmetry.

remarkably reduced from its low-temperature value because of the thermal fluctuation of spin moments at the interfacial region with MgO [11]. One way to suppress the thermal fluctuation of the interfacial moments is to choose electrode materials with very high  $T_C$ . For example, metastable bcc Co is known to have  $T_C \approx 1500$  K, and the MTJ with bcc Co electrodes has a very weak temperature dependence of the TMR ratio [18]. The values of TMR ratios at low and room temperature are 507% and 410%, respectively [18]. In this study, we have calculated  $T_C$  within the mean-field approximation (MFA). It is well known that the MFA generally overestimates  $T_C$  as it ignores the short-range spin correlation in the paramagnetic phase. A study by Zagrebin *et al.* showed that the values of  $T_C$  evaluated within the MFA in combination with LDA are in better agreement with the experimental values [57]. In Fig. 6, we plot the values of  $T_C$  evaluated from the electronic structure calculated with LDA and GGA. (Note that  $T_C$  of CoCrMnAl did not converge for GGA). Here, we also include bcc Fe and bcc Co for the sake of comparison in addition to CoCrMnZ. CoCrMnSi and CoCrMnGe have  $T_C$  values almost half that of the value of bcc Co. However, CoCrMnAl and CoCrMnGa have  $T_C$  values close to bcc Co.

These findings show that the MTJs in CoCrMnAl and CoCrMnGa could have a weaker temperature dependence of the TMR ratio.

### 1. Influence of swapping disorders

In the case of quaternary Heusler alloys, one of the major challenges is to synthesize the ordered  $Y$  structure. Various types of antisite or swapping disorders may form during its experimental fabrication. Until now our discussion has been limited to the ordered  $Y$  structure. In this section we discuss the possibility of the formation of disordered phases in terms of their total energies with respect to the ordered phase. We also discuss the influence of various types of swapping disorder on the electronic structure. Here, we consider four different types of disordered phases: (i) Co-Cr swapping disorder ( $L2_1$ -I), (ii) Mn-Z swapping disorder ( $L2_1$ -II), (iii) Mn-Cr swapping disorder ( $XA$ ), and (iv) Co-Cr and Mn-Z swapping disorder ( $B2$ ), as depicted in Fig. 7.

Figure 8 compares the relative energies of the disordered phases with respect to the ordered one. We find that the ordered  $Y$  structure is the energetically most stable, followed

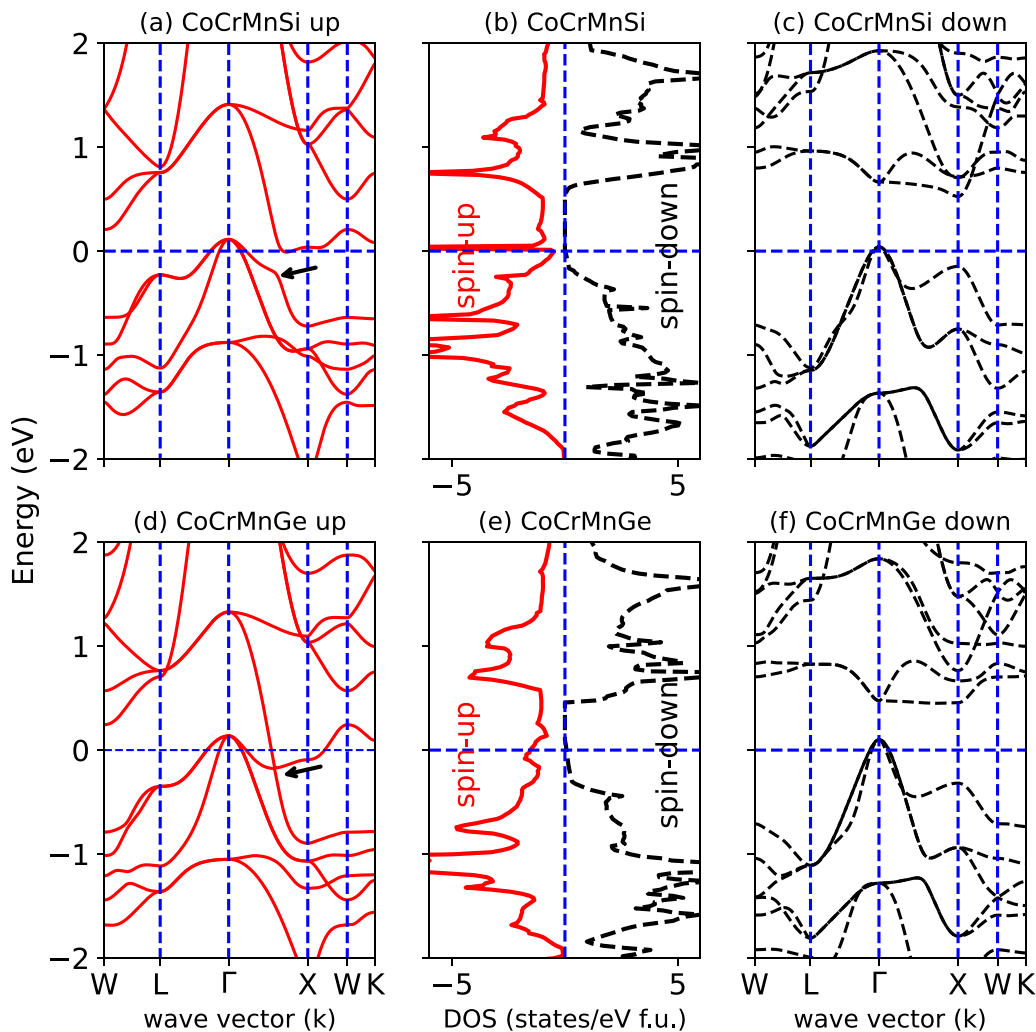


FIG. 5. Band dispersion curves and density of states for (a)–(c) CoCrMnSi and (d)–(f) CoCrMnGe. Black arrows in (a) and (d) indicate the electronic band with  $\Delta_1$  symmetry.

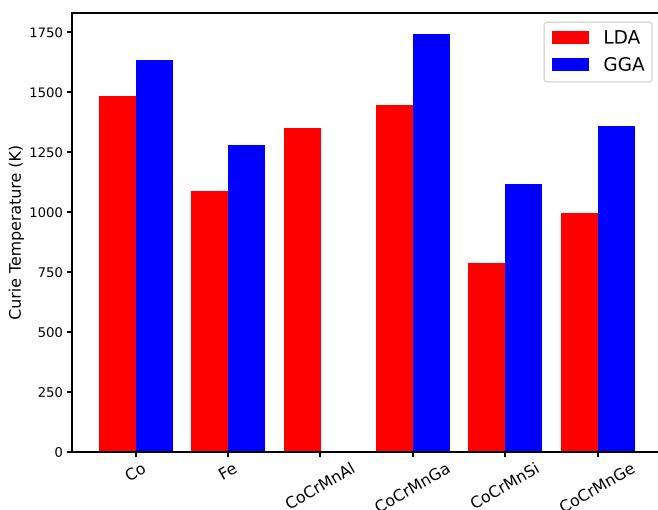


FIG. 6. Curie temperatures for (a) CoCrMnAl, (b) CoCrMnGa, (c) CoCrMnSi, and (d) CoCrMnGe, evaluated using LDA and GGA. Those for bcc Co and bcc Fe are also presented for the sake of comparison. ( $T_C$  of CoCrMnAl did not converge using GGA).

by the  $L2_1$ -I and  $XA$  types of disorder. The swapping disorders between the transition-metal elements themselves tend to be energetically less expensive and hence more likely to occur. It can be understood that all three transition elements, namely, Co, Cr, and Mn, have very close atomic numbers, atomic radii, and valence electron numbers, which could promote intermixing between them. On the other hand, the  $L2_1$ -II and  $B2$  disordered phases which involve swapping between main-group elements and the transition-metal elements, are energetically unfavorable and hence more unlikely to occur. Figure 8 also depicts the influence of various disordered phases on the total magnetic moment. It is clearly observed that the total magnetic moment is mostly robust against the swapping disorders.

As the spin polarization of conduction electrons is an important physical quantity for understanding spin-dependent transport properties, we also show the influence of swapping disorder on the spin polarization in Fig. 9. All the materials maintain high spin polarization in the disordered phases, which can also be found from the atom- and spin-resolved DOSs presented in Figs. S1– S4 of the Supplemental Material

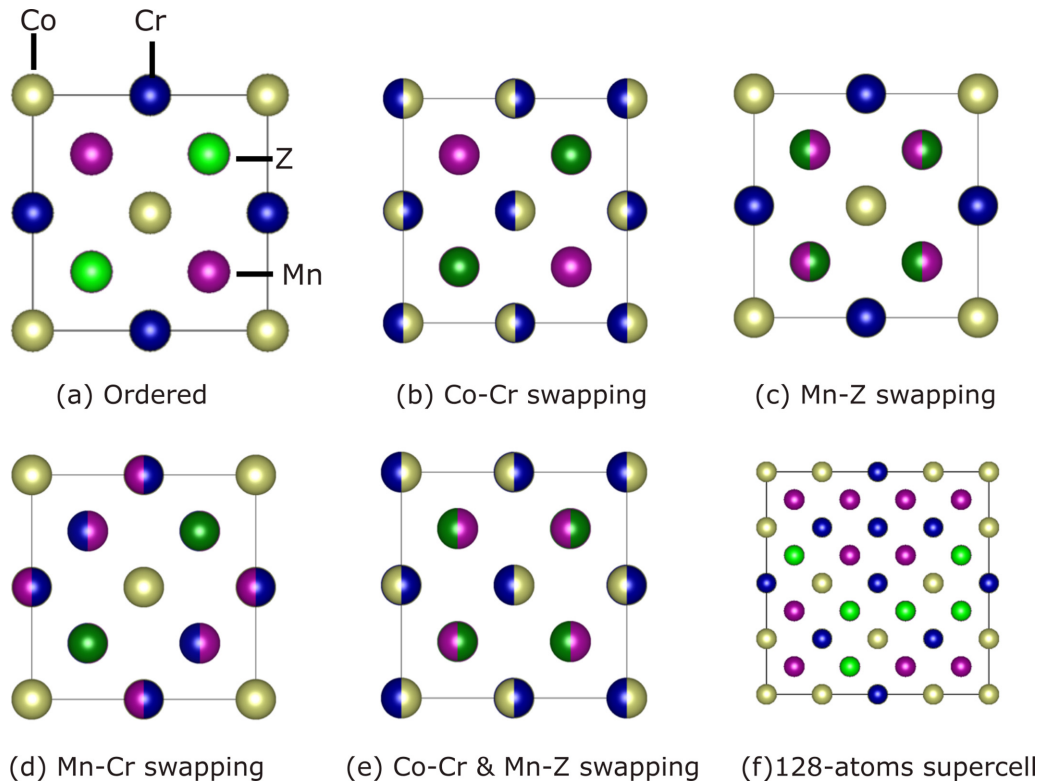


FIG. 7. Schematic representation of various atomic orderings considered: (a) Ordered,  $Y$ , (b) Co-Cr swapping,  $L_{21-I}$ , (c) Mn-Z swapping,  $L_{21-II}$ , (d) Mn-Cr swapping,  $XA$ , and (e) Co-Cr and Mn-Z swapping,  $B_2$ . (f) The atomic configuration in the SQS for the  $B_2$  phase.

[58]. Thus, we conclude that the swapping disorder does not affect spin polarization significantly.

**C. Interface with MgO**

**1. Electronic structure and stability consideration**

In this section we discuss the electronic structure of the CoCrMnZ/MgO (001) heterojunctions. For CoCrMnZ, we consider two types of terminations, namely, CoCr-terminated

and MnZ-terminated interfaces. In both cases the atoms on the terminated layer of the CoCrMnZ are located at the top of the O atom of MgO. The interfacial lattice mismatch between CoCrMnZ Heusler alloys ( $a_{opt}/\sqrt{2}$ ) and MgO (4.21 Å) is 2.2%, 1.9%, 4.7%, and 2.5% for CoCrMnAl, CoCrMnGa, CoCrMnSi, and CoCrMnGe, respectively.

Figures 10 and 11 show the DOSs of CoCrMnZ/MgO (001) heterojunctions for the CoCr- and MnZ-terminated interfaces, respectively. For both terminations high spin

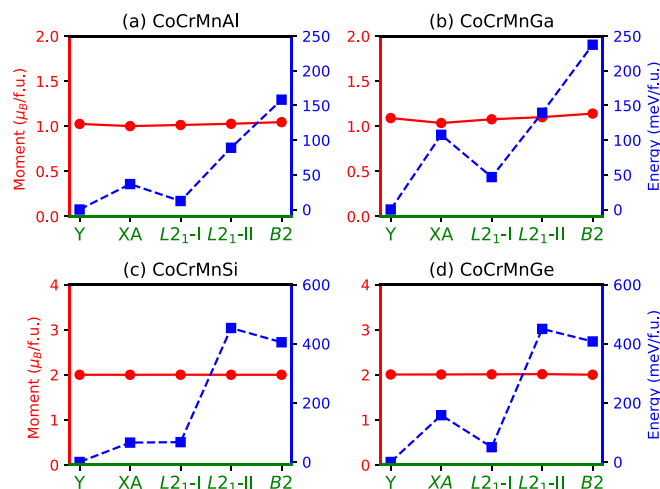


FIG. 8. Total magnetic moment (red circles) and total energy (blue squares) of ordered  $Y$  and disordered  $XA$ ,  $L_{21-I}$ ,  $L_{21-II}$ , and  $B_2$  phases for (a) CoCrMnAl, (b) CoCrMnGa, (c) CoCrMnSi, and (d) CoCrMnGe.

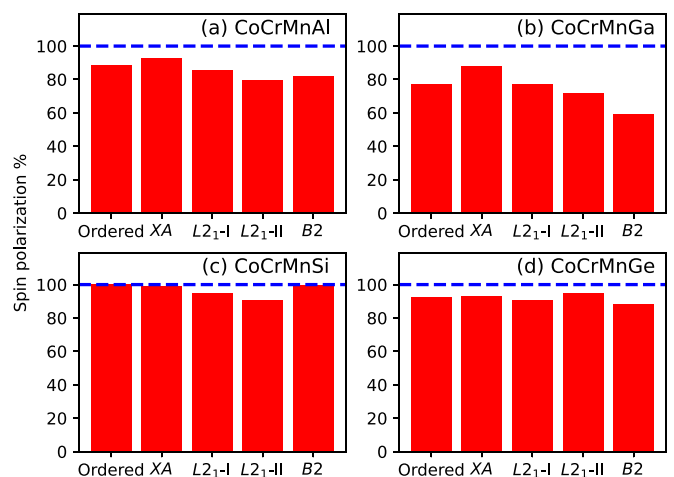


FIG. 9. Spin polarization at  $E_F$  of ordered  $Y$  and disordered  $XA$ ,  $L_{21-I}$ ,  $L_{21-II}$ , and  $B_2$  phases for (a) CoCrMnAl, (b) CoCrMnGa, (c) CoCrMnSi, and (d) CoCrMnGe.

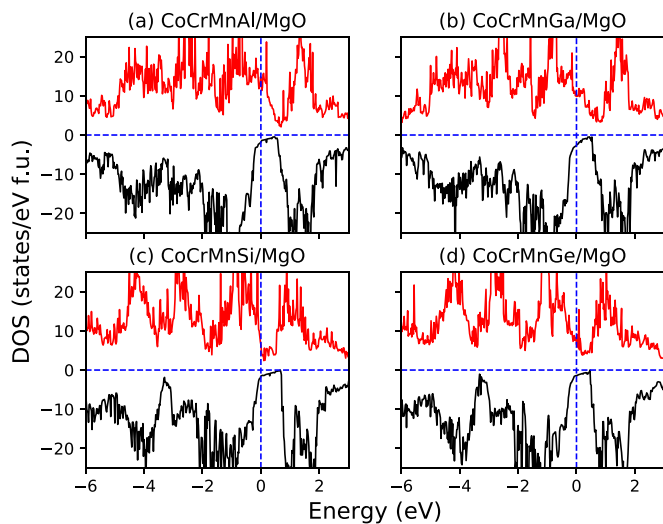


FIG. 10. Density of states (DOS) of CoCr-terminated (a) CoCrMnAl/MgO, (b) CoCrMnGa/MgO, (c) CoCrMnSi/MgO, and (d) CoCrMnGe/MgO heterojunctions.

polarization in their respective bulk phases is maintained. The values of the spin polarization in the CoCr-terminated interfaces are 77%, 59%, 61%, and 64%, respectively, for CoCrMnAl/MgO, CoCrMnGa/MgO, CoCrMnSi/MgO, and CoCrMnGe/MgO. For the MnZ-terminated interfaces the values of the spin polarization become 90%, 83%, 67%, and 41% for CoCrMnAl/MgO, CoCrMnGa/MgO, CoCrMnSi/MgO, and CoCrMnGe/MgO, respectively. We show the robustness of spin polarization against the thickness of MgO layers in Fig. S5 [58]. It is observed that the in-gap states in the minority-spin channel appear at  $E_F$  in the MnSi-terminated CoCrMnSi/MgO and MnGe-terminated CoCrMnGe/MgO heterojunctions. Further analysis shows that these in-gap

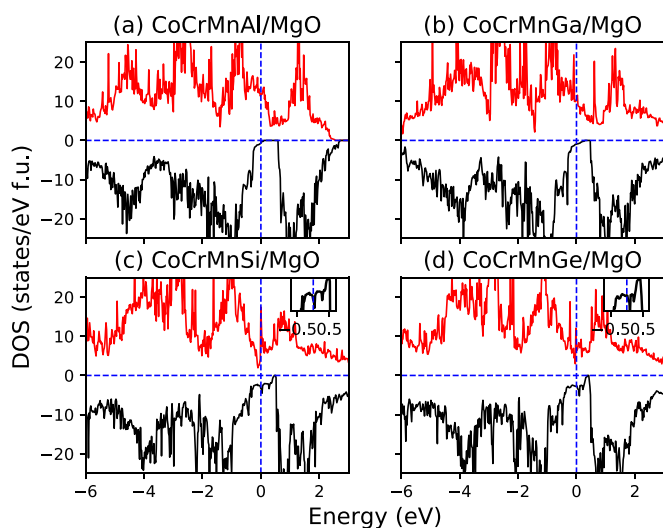


FIG. 11. Density of states (DOS) of MnZ-terminated (a) CoCrMnAl/MgO, (b) CoCrMnGa/MgO, (c) CoCrMnSi/MgO, and (d) CoCrMnGe/MgO heterojunctions. The insets in (c) and (d) show the DOS in the vicinity of  $E_F$  for the minority-spin channel.

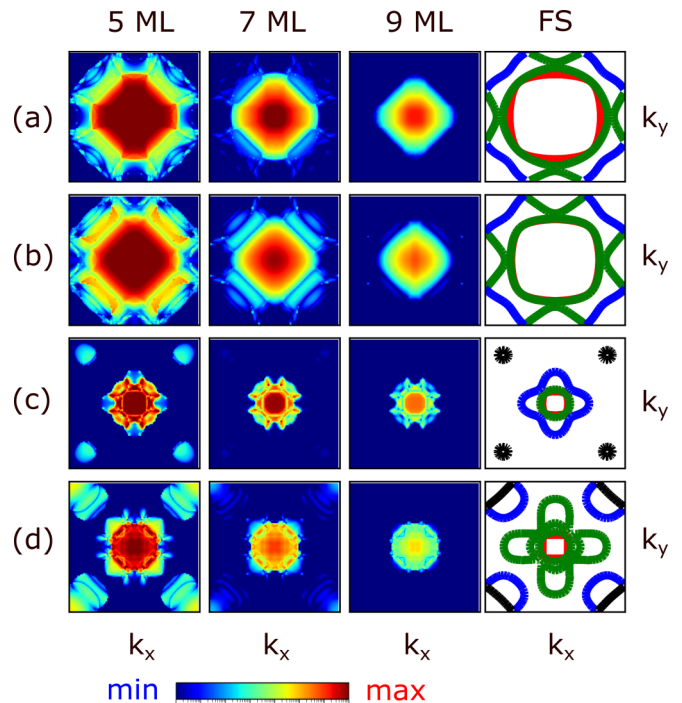


FIG. 12. In-plane wave vector ( $k_x$ ,  $k_y$ ) dependence of the majority-spin transmittance at  $E_F$  in the parallel magnetization configuration for (a) CoCrMnAl/MgO( $n$  ML)/CoCrMnAl (001), (b) CoCrMnGa/MgO( $n$  ML)/CoCrMnGa (001), (c) CoCrMnSi/MgO( $n$  ML)/CoCrMnSi (001), and (d) CoCrMnGe/MgO( $n$  ML)/CoCrMnGe (001) MTJs ( $n = 5, 7, 9$ ). The rightmost panels show the cross section of the majority-spin Fermi surface plotted using FERMISURFER [60].

states mainly arise from the interfacial Si (Ge) atoms because of their weak bonding with the nearest neighboring O atoms. This observation is quite consistent with our earlier studies on related systems [13,27,59].

Furthermore, we compare the relative stability between the CoCr- and MnZ-terminated heterojunctions using the formalism adopted in previous studies [27]. We calculate the formation energy  $E_{\text{form}}$  from the following formula:

$$E_{\text{form}} = E_{\text{total}} - \sum_i N_i E_i, \quad (2)$$

where  $E_{\text{total}}$  is the total energy of the relevant heterojunction,  $N_i$  is the number of atoms of each constituent elements, and  $E_i$  is the total energy of each element in its ground state. According to the  $E_{\text{form}}$  evaluated for both terminations, the MnZ-terminated interface is energetically favorable compared to the CoCr-terminated one. The differences in the formation energies are 1.99, 1.68, 1.31, and 1.27 eV, respectively, for the CoCrMnAl/MgO, CoCrMnGa/MgO, CoCrMnSi/MgO, and CoCrMnGe/MgO heterojunctions.

As the MnZ-terminated heterojunctions are more stable than the CoCr-terminated ones, we focus on the MnZ-terminated interface in the following study of spin-transport properties of CoCrMnZ/MgO/CoCrMnZ (001) MTJs.



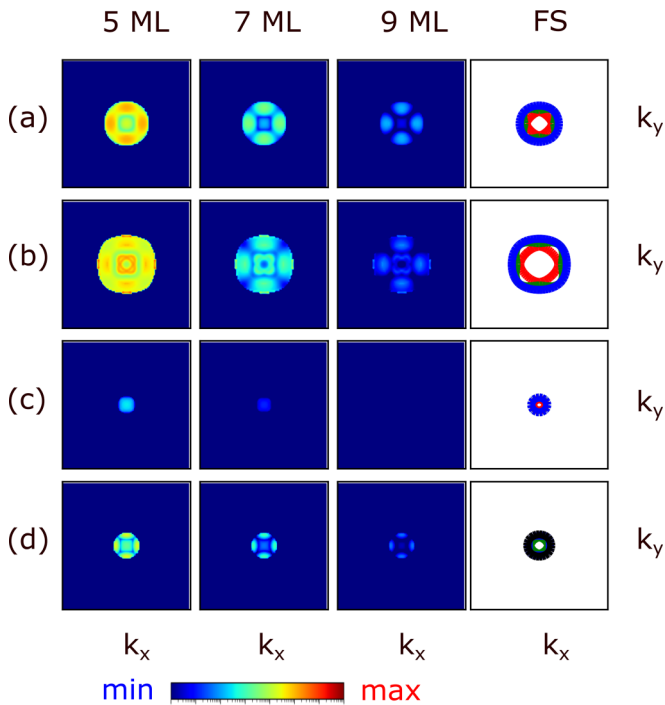


FIG. 13. In-plane wave vector ( $k_x$ ,  $k_y$ ) dependence of the minority-spin transmittance at  $E_F$  in the parallel magnetization configuration for (a) CoCrMnAl/MgO( $n$  ML)/CoCrMnAl (001), (b) CoCrMnGa/MgO( $n$  ML)/CoCrMnGa (001), (c) CoCrMnSi/MgO( $n$  ML)/CoCrMnSi (001), and (d) CoCrMnGe/MgO( $n$  ML)/CoCrMnGe (001) MTJs ( $n = 5, 7, 9$ ). The rightmost panels show the cross section of the minority-spin Fermi surface plotted using FERMISURFER [60].

## 2. Ballistic transport properties

Here, we discuss the ballistic transport properties of CoCrMnZ/MgO ( $n$  ML)/CoCrMnZ (001) MTJs in parallel and antiparallel magnetizations. In the parallel magnetization, the magnetic configuration is  $\text{Co}^\uparrow\text{Cr}^\downarrow\text{Mn}^\uparrow\text{Z}/\text{MgO}/\text{Co}^\uparrow\text{Cr}^\downarrow\text{Mn}^\uparrow\text{Z}$ ; in the antiparallel magnetization the configuration becomes  $\text{Co}^\uparrow\text{Cr}^\downarrow\text{Mn}^\uparrow\text{Z}/\text{MgO}/\text{Co}^\downarrow\text{Cr}^\uparrow\text{Mn}^\downarrow\text{Z}$ , where the arrows indicate the direction of the magnetic moment of the individual atoms. In Fig. 12, we show the in-plane wave vector ( $k_x$ ,  $k_y$ ) dependence of the electron transmission profile of CoCrMnZ/MgO ( $n$  ML)/CoCrMnZ (001) MTJs in the parallel magnetization configuration, where  $n = 5, 7, 9$ . In almost all cases, a large transmission is centered at  $(k_x, k_y) = (0, 0)$  in the two-dimensional Brillouin zone. This feature can be assigned to the presence of a partially occupied  $\Delta_1$  band in the majority-spin channel. We also found that as the MgO layers become thicker, off-center transmission vanishes, except for the transmission around  $(k_x, k_y) = (0, 0)$ . To understand the transmission profile for the MTJs for each electrode material, we show the cross section of the Fermi surface (FS) for the tetragonal unit cell of CoCrMnZ on a plane perpendicular to the (001) direction and passing through the  $\Gamma$  point. A clear correlation can be seen between the shape of the FS cross section and the transmission profile through the MgO barrier, specifically when the MgO layers are thinner.

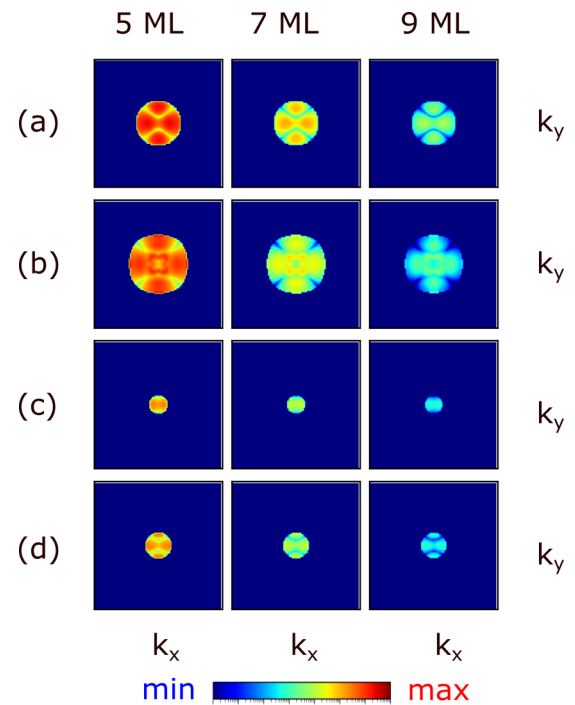


FIG. 14. In-plane wave vector ( $k_x$ ,  $k_y$ ) dependence of the majority-spin transmittance at  $E_F$  in the antiparallel magnetization configuration for (a) CoCrMnAl/MgO( $n$  ML)/CoCrMnAl (001), (b) CoCrMnGa/MgO( $n$  ML)/CoCrMnGa (001), (c) CoCrMnSi/MgO( $n$  ML)/CoCrMnSi (001), and (d) CoCrMnGe/MgO( $n$  ML)/CoCrMnGe (001) MTJs ( $n = 5, 7, 9$ ).

The minority-spin transmission probability is presented in Fig. 13 as a function of the in-plane wave vector. The minority-spin transmittance is limited only close to  $(k_x, k_y) = (0, 0)$ . We have already observed in the band structure of CoCrMnZ that the top of the valence band just touches  $E_F$  near the  $\Gamma$  point. It leads to a smaller FS for the minority-spin channel, as shown in the rightmost panels of Fig. 13, which is consistent with a narrow conduction channel for the minority-spin electrons.

Now, to discuss the spin-filtering properties of the CoCrMnZ/MgO/CoCrMnZ MTJs, the MgO-thickness dependence of the transmission profile of electrons in the antiparallel magnetization configuration is presented in Fig. 14. The transmission in the antiparallel configuration involves the tunneling of electrons from the majority-spin channel of one electrode to the minority-spin channel of the other. Here, we study symmetric MTJs, in which the electrodes on opposite sides of the barrier are identical. Thus, the transmission in the antiparallel configuration is related to the availability of both the minority- and majority-spin electronic states at  $E_F$ . In CoCrMnZ electrodes, we found a smaller FS for the minority-spin channel; thus, the transmission is also limited to the region around  $(k_x, k_y) = (0, 0)$ . As anticipated, a low value of transmittance in the antiparallel magnetization configuration is obtained here, which is required to have a higher TMR ratio of the MTJs. We evaluate the TMRs ratio of the MTJs with a 7 ML MgO barrier, which is almost equivalent to 1.5 nm of barrier thickness. The values of the TMR ratios are

quite huge, i.e., 8631%, 4597%, 70295%, and 5804% for the CoCrMnAl/MgO(7 ML)/CoCrMnAl, CoCrMnGa/MgO(7 ML)/CoCrMnGa, CoCrMnSi/MgO(7 ML)/CoCrMnSi, and CoCrMnGe/MgO(7 ML)/CoCrMnGe MTJs, respectively.

#### IV. SUMMARY

By using first-principles calculations, we found that CoCrMnZ ( $Z = \text{Al, Ga, Si, Ge}$ ) have a ferrimagnetic ground state with a very high  $T_C$ . In the respective bulk phases, they have very high spin polarization of conduction electrons, which is robust against swapping disorder. Although these systems possess a slight positive phase separation energy, the negative formation energy and the absence of imaginary frequency in the phonon dispersion curves ensure the possibility of growing these materials as thin films. We also reported a large transmission of the majority-spin electrons in the CoCrMnZ/MgO/CoCrMnZ MTJs in the parallel magnetization configuration owing to the presence of a  $\Delta_1$  band across

$E_F$ , whereas the transmission in the antiparallel magnetization configuration is remarkably low. This leads to colossal TMR ratios much higher than 1000%. Thus, we conclude that the high spin polarization of conduction electrons, the good lattice matching with MgO, and the huge TMR ratio along with very high  $T_C$ , specifically for CoCrMnAl and CoCrMnGa, could make them technologically important in spintronics device applications, which awaits experimental validation.

#### ACKNOWLEDGMENTS

This work was partially supported by CREST (Grant No. JPMJCR17J5) from Japan Science and Technology Agency (JST), the Initiative to Establish Next-Generation Novel Integrated Circuit Centers (X-NICS) (Grant No. JPJ011438) from Ministry of Education, Culture, Sports, Science and Technology (MEXT), and by Center for Science and Innovation in Spintronics (CSIS), Tohoku University. The authors thank S. Mizukami and A. Hirohata for fruitful discussions.

- 
- [1] M. Julliere, *Phys. Lett. A* **54**, 225 (1975).  
 [2] T. Miyazaki and N. Tezuka, *J. Magn. Magn. Mater.* **139**, L231 (1995).  
 [3] J. S. Moodera, L. R. Kinder, T. M. Wong, and R. Meservey, *Phys. Rev. Lett.* **74**, 3273 (1995).  
 [4] C. Chappert, A. Fert, and F. Van Dau, *Nat. Mater.* **6**, 813 (2007).  
 [5] J. Chen, Y. Lau, J. M. D. Coey, M. Li, and J. Wang, *Sci. Rep.* **7**, 42001 (2017).  
 [6] W. Lv, J. Cai, H. Tu, L. Zhang, R. Li, Z. Yuan, G. Finocchio, S. Li, X. Sun, L. Bian, B. Zhang, R. Xiong, and Z. Zeng, *Appl. Phys. Lett.* **121**, 232406 (2022).  
 [7] Y. Miura, K. Nagao, and M. Shirai, *Phys. Rev. B* **69**, 144413 (2004).  
 [8] T. Roy, D. Pandey, and A. Chakrabarti, *Phys. Rev. B* **93**, 184102 (2016).  
 [9] I. Galanakis, P. H. Dederichs, and N. Papanikolaou, *Phys. Rev. B* **66**, 174429 (2002).  
 [10] B. Hülßen, M. Scheffler, and P. Kratzer, *Phys. Rev. Lett.* **103**, 046802 (2009).  
 [11] Y. Miura, K. Abe, and M. Shirai, *Phys. Rev. B* **83**, 214411 (2011).  
 [12] Y. Miura, K. Abe, and M. Shirai, *J. Phys.: Condens. Matter* **21**, 064245 (2009).  
 [13] Y. Miura, H. Uchida, Y. Oba, K. Abe, and M. Shirai, *Phys. Rev. B* **78**, 064416 (2008).  
 [14] H. Liu, Y. Honda, T. Taira, K. Matsuda, M. Arita, T. Uemura, and M. Yamamoto, *Appl. Phys. Lett.* **101**, 132418 (2012).  
 [15] W. H. Butler, X.-G. Zhang, T. C. Schulthess, and J. M. MacLaren, *Phys. Rev. B* **63**, 054416 (2001).  
 [16] J. Mathon and A. Umerski, *Phys. Rev. B* **63**, 220403(R) (2001).  
 [17] Y. Miura, H. Uchida, Y. Oba, K. Nagao, and M. Shirai, *J. Phys.: Condens. Matter* **19**, 365228 (2007).  
 [18] S. Yuasa, T. Katayama, T. Nagahama, A. Fukushima, H. Kubota, Y. Suzuki, and K. Ando, *Appl. Phys. Lett.* **87**, 222508 (2005).  
 [19] K. Kunimatsu, T. Tsuchiya, T. Roy, K. Elphick, T. Ichinose, M. Tsujikawa, A. Hirohata, M. Shirai, and S. Mizukami, *Appl. Phys. Express* **13**, 083007 (2020).  
 [20] K. Kunimatsu, T. Tsuchiya, K. Elphick, T. Ichinose, K. Z. Suzuki, A. Hirohata, and S. Mizukami, *Jpn. J. Appl. Phys.* **58**, 080908 (2019).  
 [21] K. Elphick, K. Yoshida, T. Roy, T. Ichinose, K. Kunimatsu, T. Tsuchiya, K. Z. Suzuki, M. Tsujikawa, Y. Nagai, S. Mizukami, M. Shirai, and A. Hirohata, *Phys. Rev. Appl.* **16**, 054052 (2021).  
 [22] T. Ichinose, J. Ikeda, Y. Onodera, T. Tsuchiya, K. Z. Suzuki, and S. Mizukami, *J. Alloys Compd.* **960**, 170750 (2023).  
 [23] T. Tsuchiya, T. Roy, K. Elphick, J. Okabayashi, L. Bainsla, T. Ichinose, K. Z. Suzuki, M. Tsujikawa, M. Shirai, A. Hirohata, and S. Mizukami, *Phys. Rev. Mater.* **3**, 084403 (2019).  
 [24] T. Roy, M. Tsujikawa, T. Kanemura, and M. Shirai, *J. Magn. Magn. Mater.* **498**, 166092 (2020).  
 [25] R. Monma, T. Roy, K. Suzuki, T. Tsuchiya, M. Tsujikawa, S. Mizukami, and M. Shirai, *J. Alloys Compd.* **868**, 159175 (2021).  
 [26] Y. Onodera, K. Elphick, T. Kanemura, T. Roy, T. Tsuchiya, M. Tsujikawa, K. Yoshida, Y. Nagai, S. Mizukami, A. Hirohata, and M. Shirai, *Jpn. J. Appl. Phys.* **59**, 073003 (2020).  
 [27] T. Roy, M. Tsujikawa, and M. Shirai, *J. Phys. D* **55**, 125303 (2022).  
 [28] Enamullah, Y. Venkateswara, S. Gupta, M. R. Varma, P. Singh, K. G. Suresh, and A. Alam, *Phys. Rev. B* **92**, 224413 (2015).  
 [29] G. Kresse and J. Furthmüller, *Phys. Rev. B* **54**, 11169 (1996).  
 [30] G. Kresse and D. Joubert, *Phys. Rev. B* **59**, 1758 (1999).  
 [31] P. E. Blöchl, *Phys. Rev. B* **50**, 17953 (1994).  
 [32] J. P. Perdew, K. Burke, and M. Ernzerhof, *Phys. Rev. Lett.* **77**, 3865 (1996).  
 [33] A. Togo, L. Chaput, T. Tadano, and I. Tanaka, *J. Phys.: Condens. Matter* **35**, 353001 (2023).  
 [34] A. Togo, *J. Phys. Soc. Jpn.* **92**, 012001 (2023).

- [35] A. Zunger, S. H. Wei, L. G. Ferreira, and J. E. Bernard, *Phys. Rev. Lett.* **65**, 353 (1990).
- [36] A. van de Walle, P. Tiwary, M. De Jong, D. L. Olmsted, M. Asta, A. Dick, D. Shin, Y. Wang, L. Q. Chen, and Z. K. Liu, *CALPHAD: Comput. Coupling Phase Diagrams Thermochem.* **42**, 13 (2013).
- [37] A. I. Liechtenstein, M. I. Katsnelson, V. P. Antropov, and V. A. Gubanov, *J. Magn. Magn. Mater.* **67**, 65 (1987).
- [38] H. Ebert *et al.*, SPR-KKR, version 7.7.3, <https://www.ebert.cup.uni-muenchen.de/>; H. Ebert, D. Ködderitzsch, and J. Minár, *Rep. Prog. Phys.* **74**, 096501 (2011).
- [39] P. Lloyd and P. V. Smith, *Adv. Phys.* **21**, 69 (1972).
- [40] R. Zeller, *J. Phys.: Condens. Matter* **20**, 035220 (2008).
- [41] S. H. Vosko, L. Wilk, and M. Nusair, *Can. J. Phys.* **58**, 1200 (1980).
- [42] S. H. Vosko and L. Wilk, *Phys. Rev. B* **22**, 3812 (1980).
- [43] P. Giannozzi *et al.*, *J. Phys.: Condens. Matter* **21**, 395502 (2009).
- [44] P. Giannozzi *et al.*, *J. Phys.: Condens. Matter* **29**, 465901 (2017).
- [45] A. Smogunov, A. Dal Corso, and E. Tosatti, *Phys. Rev. B* **70**, 045417 (2004).
- [46] K. Momma and F. Izumi, *J. Appl. Crystallogr.* **44**, 1272 (2011).
- [47] Enamullah, D. D. Johnson, K. G. Suresh, and A. Alam, *Phys. Rev. B* **94**, 184102 (2016).
- [48] Q. Gao, I. Opahle, and H. Zhang, *Phys. Rev. Mater.* **3**, 024410 (2019).
- [49] J. Nehra, V. D. Sudheesh, N. Lakshmi, and K. Venugopalan, *Phys. Status Solidi RRL* **7**, 289 (2013).
- [50] V. N. Uvarov, Y. V. Kudryavtsev, E. M. Rudenko, N. V. Uvarov, A. E. Perekos, M. P. Melnik, and V. Y. Tarenkov, *J. Appl. Phys.* **134**, 114401 (2023).
- [51] S. Nepal, R. Dhakal, I. Galanakis, S. M. Winter, R. P. Adhikari, and G. C. Kaphle, *Phys. Rev. Mater.* **6**, 114407 (2022).
- [52] K. J. Caspersen, A. Lew, M. Ortiz, and E. A. Carter, *Phys. Rev. Lett.* **93**, 115501 (2004).
- [53] J. A. Rayne and B. S. Chandrasekhar, *Phys. Rev.* **122**, 1714 (1961).
- [54] W. Voigt, *Ann. Phys. (Berlin, Ger.)* **274**, 573 (1889).
- [55] S. Ener, J. Neuhaus, W. Petry, R. Mole, K. Hradil, M. Siewert, M. E. Gruner, P. Entel, I. Titov, and M. Acet, *Phys. Rev. B* **86**, 144305 (2012).
- [56] A. Kundu, M. E. Gruner, M. Siewert, A. Hucht, P. Entel, and S. Ghosh, *Phys. Rev. B* **96**, 064107 (2017).
- [57] M. A. Zagrebin, M. V. Matyunina, V. V. Sokolovskiy, and V. D. Buchelnikov, *J. Phys.: Conf. Ser.* **1389**, 012087 (2019).
- [58] See Supplemental Material at <http://link.aps.org/supplemental/10.1103/PhysRevMaterials.7.104410> for the density of states of ordered and disordered phases of CoCrMnZ alloys, and MgO thickness dependence of spin polarizations of CoCrMnZ/MgO heterojunctions.
- [59] T. Roy, M. Tsujikawa, and M. Shirai, *J. Phys.: Condens. Matter* **33**, 145505 (2021).
- [60] M. Kawamura, *Comput. Phys. Commun.* **239**, 197 (2019).